Depth determination of the Moho interface beneath the Tibetan plateau and other areas of China[*]

Youshun Sun[1,2]   Diming Yu[3]   M Nafi Toksöz[2]

F Dale Morgan[2]   Xiyu Wang[2]   Jinrong Su[3]   and   Jun Liu[2,4]

[1] *State Key Laboratory of Geodesy and Earth's Dynamics, Institute of Geodesy and Geophysics, Chinese Academy of Sciences, Wuhan 430077, China*

[2] *Department of Earth, Atmospheric and Planetary Sciences, Massachusetts Institute of Technology, Cambridge, MA 02139, USA*

[3] *Earthquake Administration of Sichuan Province, Chengdu 610041, China*

[4] *School of Civil Engineering and Architecture, Wuhan University of Technology, Wuhan 430070, China*

Abstract   We apply the adaptive moving window method of Sun et al. to the most recent catalog data and the data recorded by portable stations to construct the velocity structure of the crust and upper mantle, and to determine the depth of the Moho interface beneath the Tibetan plateau and other areas of China. We first select 2 600 locations in the study region with 1° intervals, then at each location invert for a five-layer 1-D P-wave velocity model from the surface down to the uppermost mantle by performing a Monte Carlo random search. The Moho depth at each location is then determined, and the Moho interface beneath the study region is obtained through proper interpolation with certain smoothing. Compared to depths obtained by previous studies, our results show more accurate Moho depths in the Tibetan plateau, Tianshan region and other areas of the study region.

Key words: **Moho depth; Moho interface; Tibetan plateau**

CLC number: P315.2   **Document code**: A

1 Introduction

The Moho discontinuity, the boundary between the Earth's crust and mantle, is known to exist everywhere beneath the Earth's surface. Named after the pioneering Croatian seismologist Andrija Mohorovičić, the Moho interface separates both the oceanic crust and continental crust from the underlying mantle. The Moho mostly lies entirely within the lithosphere, and only beneath mid-ocean ridges does it define the lithosphere-asthenosphere boundary (McLeish, 1992). The Moho discontinuity was first identified in 1909 by Mohorovičić when he observed that seismograms from shallow-focus earthquakes had two sets of P-waves and S-waves, one that followed a direct path near the Earth's surface and the other refracted by a high velocity medium (McLeish, 1992).

The Moho discontinuity is 5 to 10 km below the ocean floor and 20 to 70+ km beneath typical continents, with an average of 35 km beneath them (Monroe and Wicander, 2008). Determination of Moho depth has been challenging due to the fact that Moho depth and crustal velocities are trade-off parameters. To correctly invert for Moho depth using seismic travel time data, it is necessary to first obtain accurate crustal velocities of the study region.

The Tibetan plateau is one of the most seismically active and complicated areas in the world. The Moho depth beneath Tibet has been identified at ~45–78 km (Liang et al., 2004; Hearn et al., 2004; Sun et al., 2004; Sun and Toksöz, 2006; Pei et al., 2007), indicating that

the Moho undulations beneath Tibet are much more vigorous compared to the Moho interface beneath other areas in China. Therefore, due to these variations across the Tibetan plateau, determining the Moho depth is particularly challenging.

The available P-wave velocity models of the crust and upper mantle in Tibet and other areas of China have been obtained using different approaches. The models based on surface waves are generally large-scale models that contain information about the deep structure of the Earth (Shapiro and Ritzwoller, 2002; Stevens et al., 2001; Huang et al., 2003; Wu et al., 1997; Lebedev and Nolet, 2003; Song et al., 1991). Although CRUST 2.0 (Bassin et al., 2000) was compiled by tomographic inversion, there are too few deep seismic soundings (DSSs) from which refraction data are obtained to provide detailed models for the areas with DSS data. Regional P-wave travel-time tomography by Liu et al. (1990) and Xu et al. (2002) showed the crustal and upper mantle structure beneath China over a large scale. Detailed crustal structures are not shown in these models. The Pn and/or Sn models by Hearn et al. (2004), Liang et al. (2004) and Pei et al. (2007) show detailed

velocity models at the Moho interface. Despite these efforts, the Moho depth was not accurately inverted in these models.

For reliable determination of the Moho depth beneath Tibet, we use the most recent earthquake catalog given in the *Annual Bulletin of Chinese Earthquakes* (*ABCE*) from 2000 to 2010 (Institute of Geophysics, China Earthquake Administration (IG-CSB hereinafter), 2000–2010) and apply the adaptive moving window (AMW) method by Sun et al. (2004) to construct velocity models and simultaneously obtain accurate depths to the Moho.

2 Data and method

We use the earthquake phase data from January 2000 to December 2010, given in the *ABCE* (IG-CSB, 2000–2010) and the data recorded by portable stations (Pei et al., 2007). In this combined database there are 30 000 earthquakes, 400 stations, and 1 200 000 ray paths in the Tibetan plateau and other areas of China. Figure 1 shows the earthquake epicenters, stations, and ray paths in the study region.
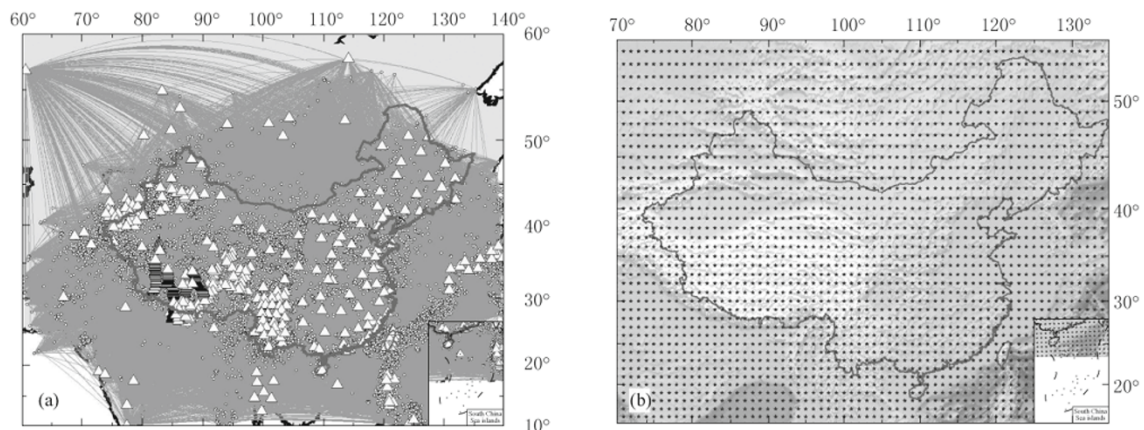

Figure 1   (a) Locations of 30 000 earthquakes (dots), 400 stations (triangles), and 1 200 000 ray paths in Tibet and other areas of China. (b) 2 600 points (stars) in Tibet and other areas of China.

Sun (2001), Sun et al. (2004) and Sun and Toksöz (2006) relocated the *ABCE* events from 1990 and 2002 and obtained very small epicentral improvement. Therefore we used the source locations given in the *ABCE* for our P-velocity model inversion. Our goal is to obtain 1-D velocity models of crust and uppermost mantle, and thereby to determine the Moho depth in the study region based on these travel-time data.

Similar to Sun et al. (2004), we selected 2 600 points distributed on a 1° grid in the study region (shown in Figure 1). As shown in Figure 2, at each point, a 1-D velocity model is obtained by fitting first arrivals

(Pg or Pn) within a window (region) centered at the point. The minimum size of each window was chosen to be 4°×4° (latitude, longitude) to guarantee sufficient Pn ray paths. The window size is increased until the required minimum numbers of Pg and Pn ray paths are included. Every 1-D velocity model consists of four layers of crust and one layer of upper mantle (shown in Figure 3). The top layer is the sediment layer, and its thickness is taken from Bassin et al. (2000). The other three crustal layer thicknesses, four P-wave velocities in the crust, and the Pn velocities are the eight parameters to be inverted with a Monte Carlo approach.
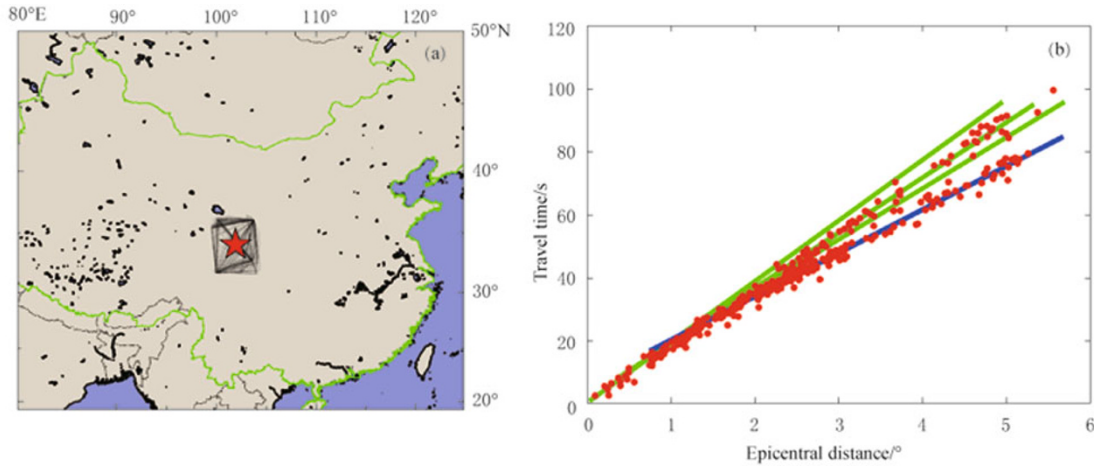
Figure 2 (a) Ray paths selected in the window centered at (102°E, 34°N). The red star indicates the center of the window. (b) Observed travel-times at (102°E, 34°N) are plotted in red dots and the calculated travel-times are plotted in green (crust) and blue (uppermost mantle) lines.
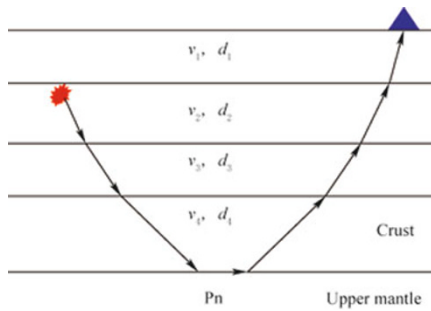

Figure 3 4 layers of crust and one-layer of uppermost mantle at each location.

The first step in the inversion is to choose travel-times. The travel-times reported at each station from an earthquake contain many phase arrivals. We use only the first arrivals in our inversion. Figure 4 shows the first arrival travel-times in China within epicentral distances of 20°. Some of the first arrivals at large distances are Pg arrivals instead of Pn. We believe those Pn arrivals were missing in the report as they might be too weak to pick. We choose all the first arrivals for the events and stations located within the window centered at each point. The size of adaptive windows is selected to ensure a minimum of 300 travel-times, including at least 100 Pn arrivals at each point. The minimum window size is 4°×4° and larger windows are used around some points so that there are at least 200 Pg and 100 Pn arrivals inside the window. In a few cases where data are sparse, the window size is as large as 15°×15° and at least 50 Pg and 20 Pn arrivals are selected in each window. The maximum epicentral distance between a source and a receiver for the entire study area is restricted to 8°.
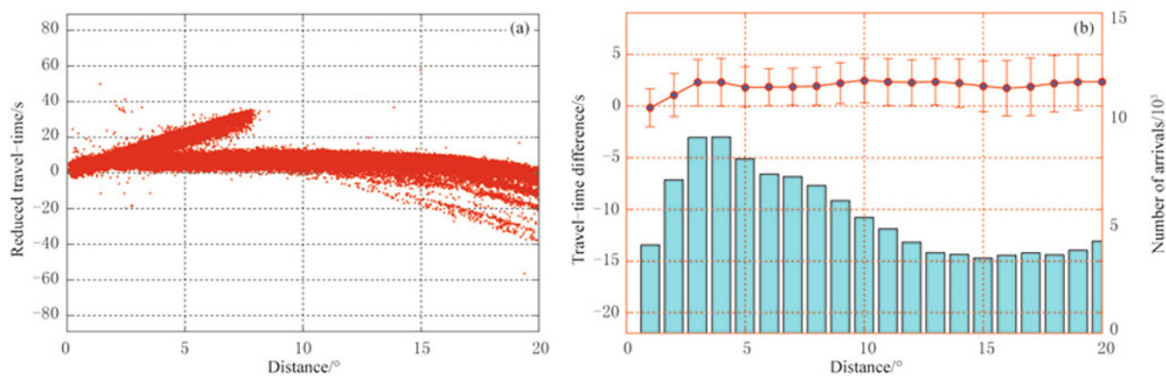

Figure 4 (a) The first arrival travel-times (reduced) in China within distances of 20°. (b) Averaged travel-time difference between the observed and calculated times based on the IASP model. The cyan bars show the number of arrivals over which the averages are taken.

The second step is to find a 1-D velocity model for each window using a Monte Carlo algorithm. As we mentioned earlier, every 1-D model contains eight parameters to be constrained from the travel-times. For each iteration, the Monte Carlo algorithm randomly selects each variable from within some preset bounds to compose a 1-D model. Pn and Pg travel-times are calculated based on the selected 1-D model and the existing event locations in the *ABCE*. Event locations are not changed from those in the catalog. Travel-time residuals for the first-arrival Pg and Pn are then obtained, and the Monte Carlo search continues until the maximum number of iterations is reached. The optimal model is the one with minimum root mean square (RMS) error. Each 1-D model is determined by 100 thousand iterations.

The search range for each variable is set a priori based on our knowledge of the model. We use the results by Sun et al. (2004) and the Pn results by Pei et al. (2007) as a guide to set bounds for the variables. The Monte Carlo search range for Pn is limited to ± 0.2 km/s of the Pei's Pn velocity. For the points not covered by their model, the Pn bound is set to [7.6, 8.3] km/s. Bounds for the thickness of each layer in the crust are generally between 0 and 20 km. The general bounds for the four crust velocities are [4, 5], [5, 6.2], [6.3, 6.6], and [6.6, 7.4] km/s. The bounds are ± 5 km of Sun et al. (2004)'s layer thickness or ± 0.5 km/s of the Sun et al. (2004)'s layer velocities.

The first arrivals at distances greater than each critical distance are Pn phases. It is possible that some observed first arrivals at large distances are Pg arrivals instead of Pn. We separate Pn and Pg phases at large distances based on the slope of the travel-time curve to avoid calculating residuals between observed Pg arrivals and calculated Pn arrivals.

The third step is to apply an adaptive moving window to all points to obtain a 1-D velocity profile at each of the 2 600 points. The 1-D velocity profile at each point inverted from the phase data inside the moving window is not exactly the velocity profile at that point, it is rather the averaged velocity profile in the window area surrounding the point. Profiles obtained from windows with large size are averaged over large areas. The points are located at 1° intervals. We up-sample all the points by a factor of 5 to a 0.2° interval using linear interpolation. Both velocity and thickness of each layer are interpolated. The up-sampling is accomplished using a Gaussian function with a half-length of 8 points to smooth all the models horizontally at each layer.

After all the up-sampled 1-D models were smoothed, we select and combine the original 2 600 1-D models to obtain an equivalent 3-D model.

3 Results and analysis

Performing the AMW method in the study area, we obtain a 3-D P-velocity model of the crust and uppermost mantle. Figure 5 shows the crustal thickness and Pn velocity in China. Figure 6 shows horizontal velocity profiles at different depths beneath China and the surrounding area. The lateral heterogeneity of the crust
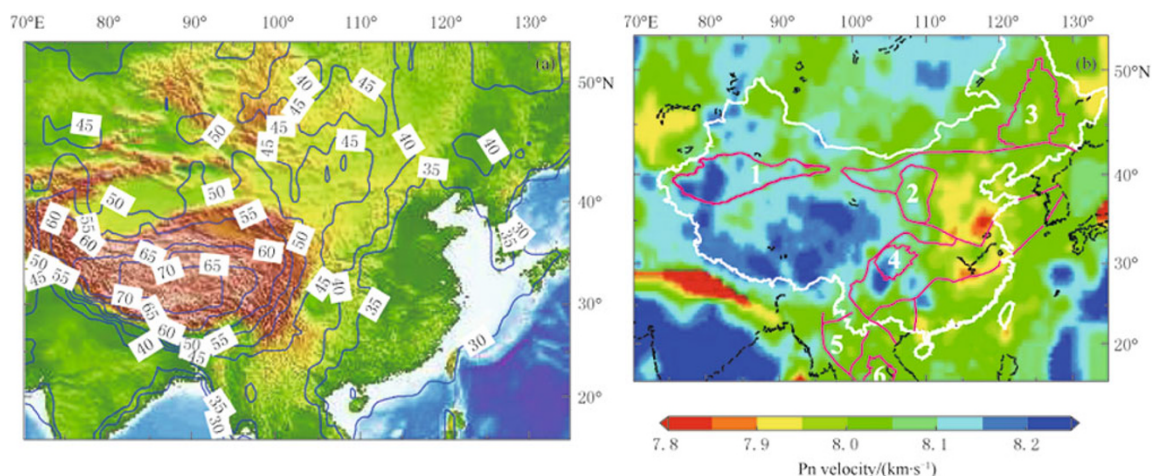

Figure 5   Contour plot of crustal thickness in China area (a) and Pn velocity in China area (b). 1. Tarim basin; 2. Ordos basin; 3. Songliao basin; 4. Sichuan basin; 5. Shan-Thai block; 6. Khorat basin.
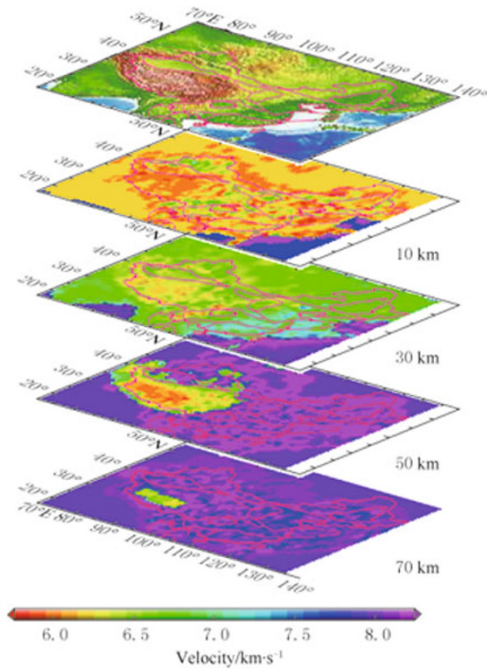
Figure 6 Horizontal velocity profiles at different depths in China and the surrounding area (the top image shows the topography). Images are shown with a common color scale.

and upper mantle beneath China is shown clearly in Figure 6. The 3-D velocity model obtained by quilting the 1-D velocity profiles correlates well with the tectonic regions. The velocity images at a depth of 50 km show that the crust of the Chinese continent is divided into two parts approximately by the 102.5°E longitude (Liu et al., 1990). In the western part, the crust is thicker and crustal velocities are lower than those in the eastern part. The 3-D velocity model indicates the crust beneath the Precambrian regions, including the Tarim basin, Sichuan basin, Ordos basin, and Songliao basin, has higher-than-average velocity. The Bohai Gulf shows both slow and fast velocity anomalies due to a Cenozoic rift system through the gulf (Sun et al., 2004). The northern part of the South China block is slower than the southern part in the lower crust and the difference is small in the uppermost mantle. The Indochina block shows a low-velocity anomaly in the crust and the uppermost mantle that is consistent with volcanism.

As shown in Figure 3, at each point, nine parameters represent a 1-D model with a four-layer crust and one-layer uppermost mantle. Eight of them are estimated by fitting first arrivals within a window centered at the point. In this section, we discuss the robustness of the random search, the uncertainty analysis, and the resolution and accuracy. We also compare our models obtained by random search with those from other researchers.

3.1 Robustness of Monte Carlo search fit

After the layered model is set up, the distances and travel-times can be calculated according to the formulas listed in Sun (2001). Based on the observed travel-times in the window centered at a point, the best eight parameters that fit the data with the minimum RMS error can be found by the Monte Carlo method (random search). The steps of a random search are as follows:

Step 1: Choose parameter ranges.

Step 2: Choose a random number, scale the [0, 1] random number to the parameter interval $[\beta_{\min}, \beta_{\max}]$, and repeat for all parameters.

Step 3: Calculate theoretical arrival time.

Step 4: Compare theoretical (T_{mod}) and observed (T_{obs}) data. The data residual ΔT is defined to be ($T_{\mathrm{mod}} - T_{\mathrm{obs}}$).

Step 5: Stop if residual misfit is small or after $n_{\max}$ trials. The residual misfit is measured by the RMS error and calculated as follows:

$$\mathrm{RMS} = \sqrt{\frac{\Sigma \Delta T^2}{N}},$$

where N is the number of observations.

Step 6: Keep parameter sets associated with small residuals.

Step 7: Repeat step 2 if residuals is large or if $n_{\max}$ is not reached.

The random search is stopped if RMS is smaller than the tolerance ε, otherwise it is kept going to the maximum iteration number, $n_{\max}$. With the random search method one can be reasonably certain of uniqueness if $n_{\max}$ goes to infinity and/or ε goes to zero. The RMS error will go to the true minimum and the parameters go to the global solution. The question is if the optimal models are obtained by limited iterations ($n_{\max}$) instead of infinity, how can we guarantee that these models are the best?

We selected a few locations in the study region and searched for 1-D models with both 100 thousand and 50 million runs. The best models found with 100 thousand runs are exactly the same as the ones with 50 million runs. Our random searches converge at around 100 thousand runs or less because there are limited travel-times for each location. We also ran 50 thousand runs for all the selected 2 600 points to guarantee the robustness of the random search fit.

The velocity models obtained at each location are the averaged ones in the area surrounding each point.

One can imagine that the velocity models obtained at neighboring locations are similar due to a large amount of shared ray paths. To test this, we select a central location at (102°E, 35°N) in the middle of China and compare the ray paths, inverted models, and travel-time fitting at the center with those that are one degree, three degrees and 10 degrees distance from the center in both longitude and latitude. The locations are shown in Figure 7.

Figures 8 through 10 show the ray paths for the locations surrounding the center point (102°E, 35°N) with one degree apart, three degrees apart and ten degrees apart, respectively. Figures 11 through 13 show the results of travel-time fitting. We can see that the travel-time data are well fit for all locations. The inverted velocity models are shown in Figures 14 through 16. Figure 14 shows that the four velocity models that are one degree away from the center are very close to the velocity model at the center. When the distance between the locations and the center increases, the velocity models become more uncorrelated.
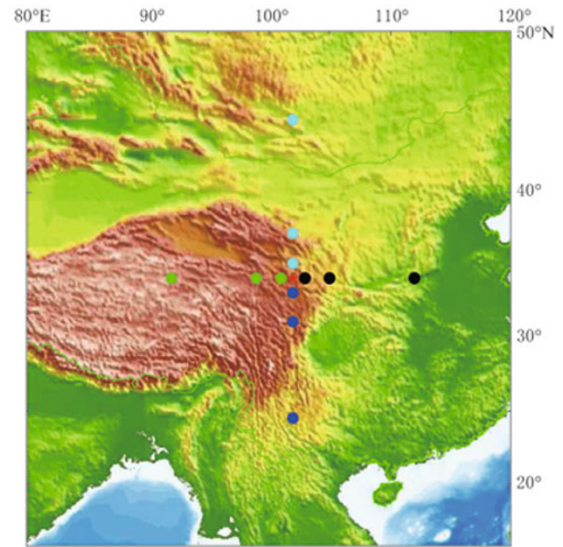
Figure 7   Selected locations with one degree, three degrees and 10 degrees distance from the center location (102°E, 35°N). The center location is shown in red star and other locations are shown in circles: blue (south), cyan (north), green (west) and black (east).
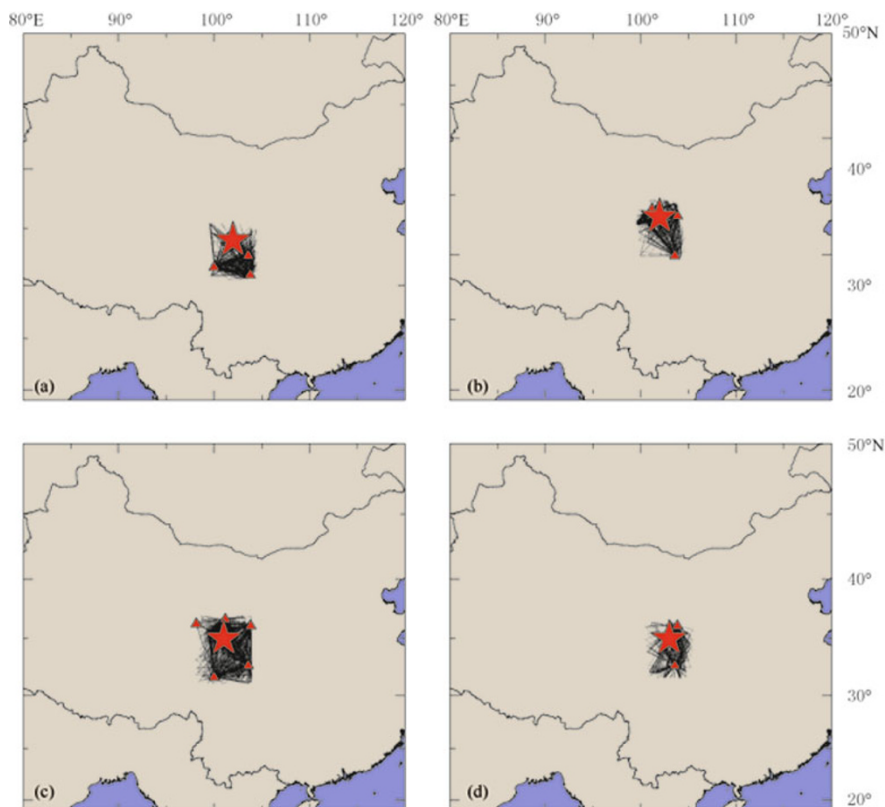

Figure 8   Ray paths at locations (102°E, 34°N) (a), (102°E, 36°N) (b), (101°E, 35°N) (c) and (103°E, 35°N) (d). The locations are shown in red stars and stations are in red triangles.
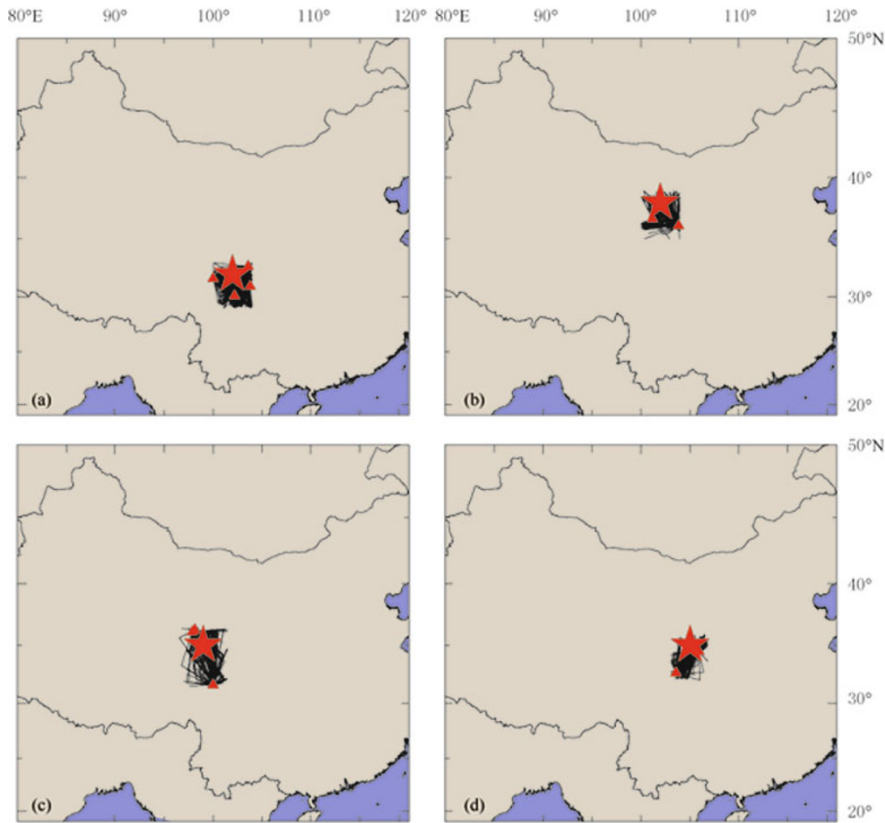
Figure 9   Ray paths at locations (102°E, 32°N) (a), (102°E, 38°N) (b), (99°E, 35°N) (c) and (105°E, 35°N) (d). The locations are shown in red stars and stations are in red triangles.

Sun (2001) showed that Monte Carlo inversion could exactly recover the velocity models from synthetic seismic data with no noise added. For the models with noise added, a random search also reduces the uncertainty of coupled parameters. Because we know that the origin time and depth of an event are trade-off parameters, we found the true depths of three explosions by using the Monte Carlo method to fit the travel-time data. We also ran the least squares location program (Hypoinverse) and saw that, in general, the depths located were a few kilometers off.

3.2   Uncertainty analysis

The best model at each location is obtained by minimizing the RMS misfit of the travel-time data. From the previous section, we know that the Monte Carlo fit is very robust when the number of iterations is 100 thousand or above. Another important question to ask is what is the uncertainty in each "best" model?

Unlike other inversion methods such as least squares (LS), in which error estimates can be evaluated based on the travel-time misfit and derivative matrix, there are no simple ways to evaluate the model errors by the Monte Carlo search fit. We first estimate the

uncertainty of the models obtained from the synthetic travel-times.

Figure 17 shows a two-layer model with a synthetic event on the surface of the Earth. The crust and the uppermost mantle are separated by a dipping Moho. There are only three parameters to represent the 1-D model at the source location. Those parameters are the Moho depth, the averaged crust velocity and the averaged velocity in the uppermost mantle. We set the Moho depth (D) beneath the event to 40 km, the averaged crust velocity (V_1) is 6.5 km/s, and the averaged Pn velocity (V_2) is 8.0 km/s.

Table 1 shows the standard deviations of the three parameters in different ranges of the dipping angle (α)

Table 1   The standard deviations (σ) of the three parameters (D, V_1 and V_2) in different ranges of the dipping angle (α) of the Moho

α	σ_D/km	σ_{V1}/(km·s^{-1})	σ_{V2}/(km·s^{-1})
0°	0	0	0
[0°, 5°]	1	0.08	0
[5°, 10°]	2	0.16	0.03
[10°, 15°]	3	0.25	0.06
[15°, 30°]	4	0.28	0.12
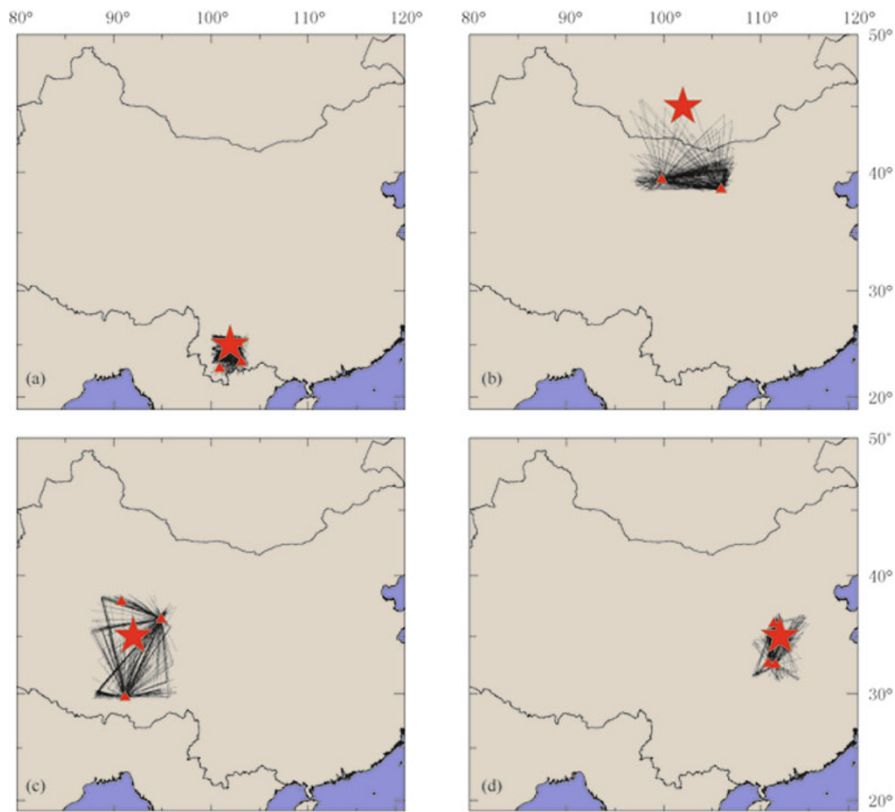
Figure 10 Ray paths at locations (102°E, 25°N) (a), (102°E, 45°N) (b), (92°E, 35°N) (c) and (112°E, 35°N) (d). The locations are shown in red stars and stations are in red triangles.
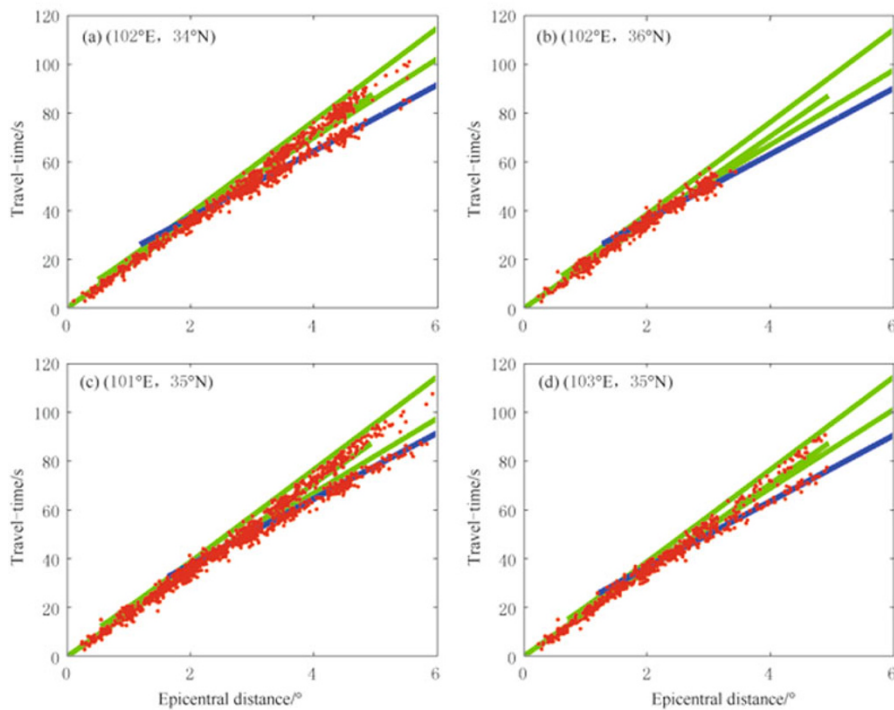
Figure 11 Travel-time fitting at locations (102°E, 34°N) (a), (102°E, 36°N) (b), (101°E, 35°N) (c) and (103°E, 35°N) (d). The observed travel-times are plotted in red dots and calculated travel-times are plotted in green (crust) and blue (uppermost mantle) lines.
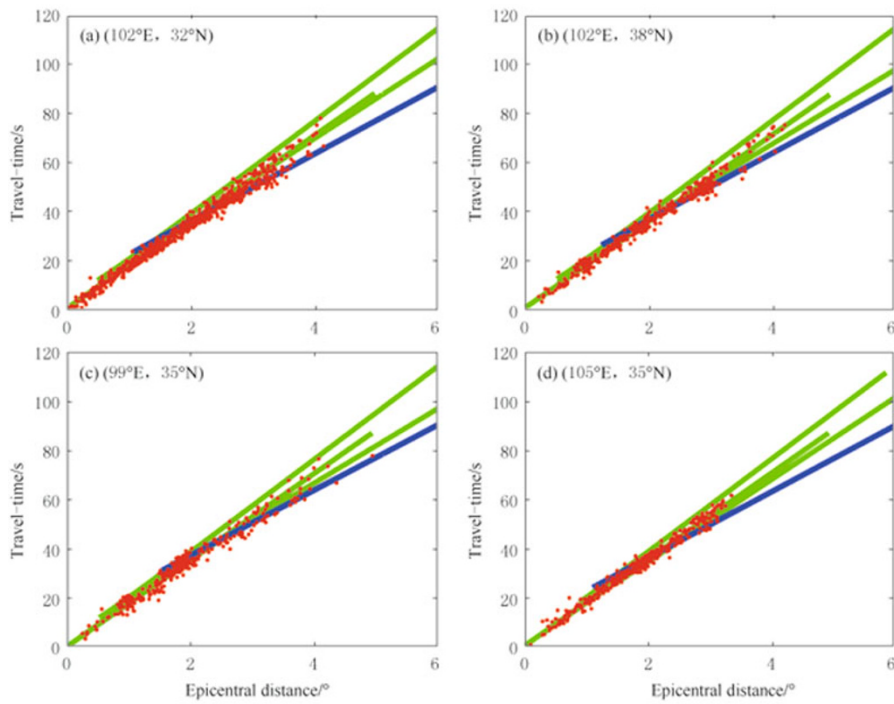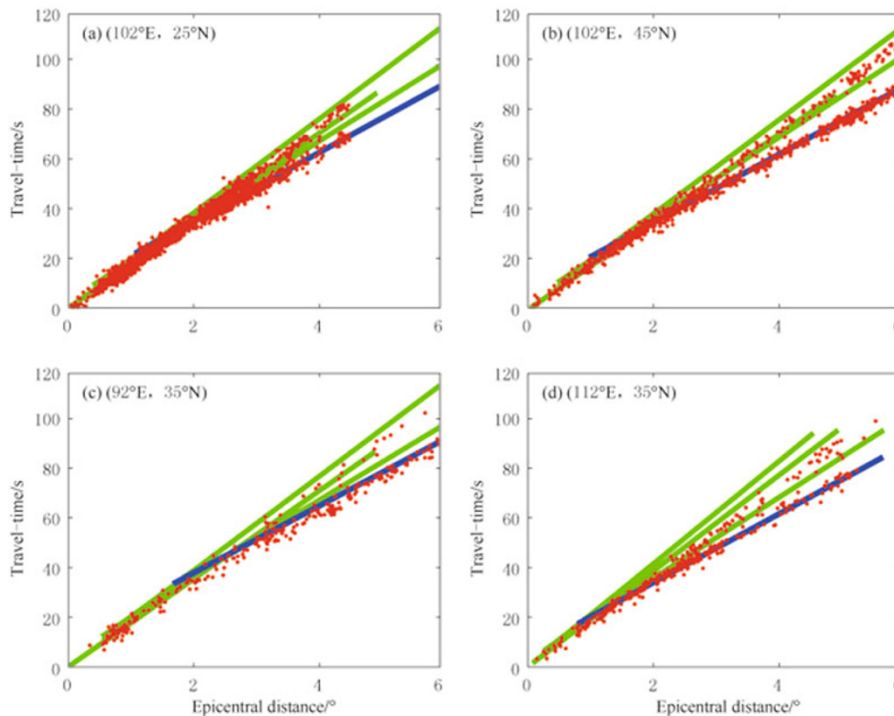
Figure 12 Travel-time fitting at locations (102°E, 32°N) (a), (102°E, 38°N) (b), (99°E, 35°N) (c) and (105°E, 35°N) (d). The observed travel-times are plotted in red dots and calculated travel-times are plotted in green (crust) and blue (uppermost mantle) lines.
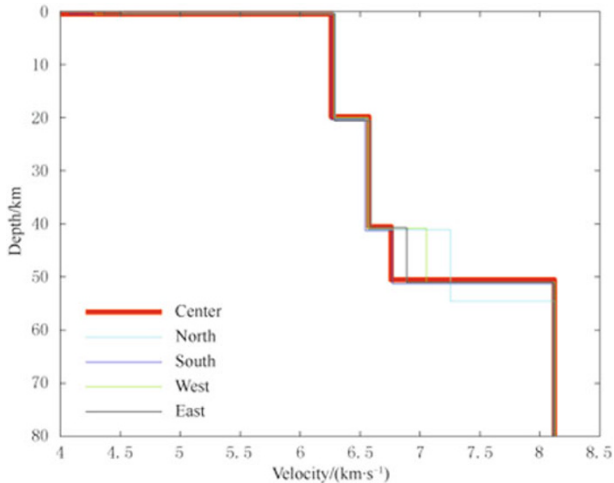

Figure 13 Travel-time fitting at locations (102°E, 25°N) (a), (102°E, 45°N) (b), (92°E, 35°N) (c) and (112°E, 35°N) (d). The observed travel-times are plotted in red dots and calculated travel-times are plotted in green (crust) and blue (uppermost mantle) lines.

Figure 14 Velocity models at locations (102°E, 36°N), (102°E, 34°N), (101°E, 35°N) and (103°E, 35°N).
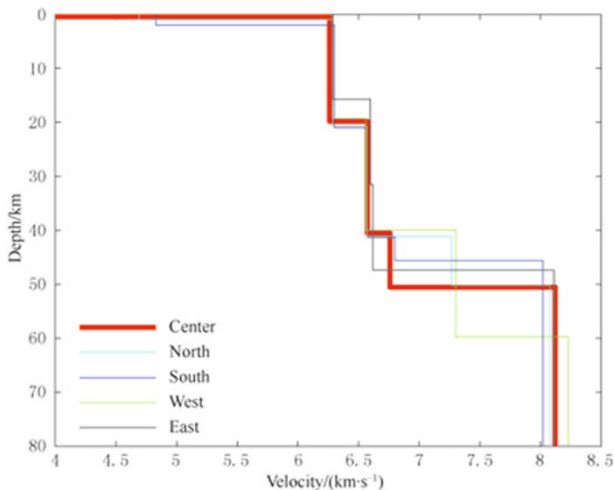

Figure 15 Velocity models at locations (102°E, 32°N), (102°E, 38°N), (99°E, 35°N) and (105°E, 35°N).

of the Moho interface. The standard deviations of all the three parameters increase when the dipping angle increases. The estimated crustal velocity carries larger uncertainties than the Pn velocity. As discussed in Sun et al. (2004), the dipping angles of the Moho interface in China are smaller than 3° in a region of 4°×4° or larger. The uncertainties of all the three parameters are smaller than one percent.

We can also understand the uncertainty in each final model by comparing each best model with other sub-optimal models (i.e. those with bigger RMS error) in the same location. We choose the same 12 points plotted in Figure 7 as the locations for model comparisons. At each location, the 10 best models based on the RMS error are selected and plotted in Figure 18. The

best models with the minimum RMS error are shown in magenta. We can see that at most locations the top ten models are close to each other. For the locations at (102°E, 36°N), (102°E, 38°N), (105°E, 35°N) and (102°E, 45°N), there are slightly larger differences in the lower crust between the models. The standard deviation (STD) of the velocity in the lower crust is from 0.05 to 0.19 km/s, while the STD range is [0.01, 0.14] in the upper crust and [0.02, 0.09] in the middle crust. The STD range of the uppermost mantle is [0.01, 0.03] due to the constraints we applied.
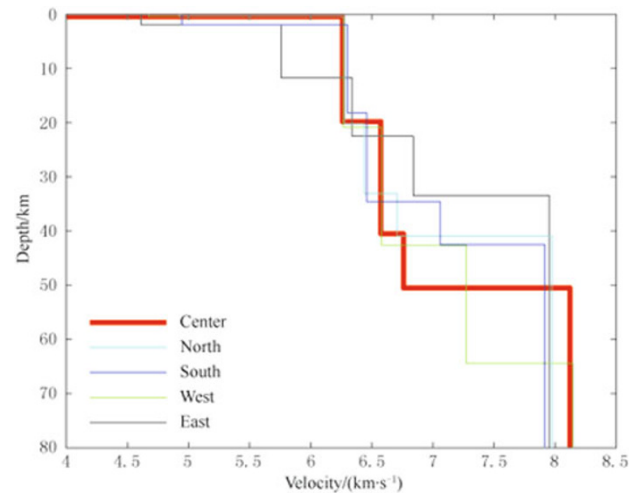

Figure 16 Velocity models at locations (102°E, 25°N), (102°E, 45°N), (92°E, 35°N) and (112°E, 35°N).
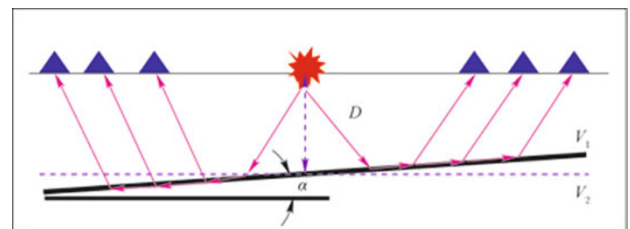

Figure 17 A synthetic event on the surface of the Earth. D is the Moho depth at the source location. V_1 is the averaged crustal velocity and V_2 is the averaged uppermost mantle velocity in the source area.

Based on the best models at the selected 12 locations, an averaged model for the entire China area is shown in Figure 19. From this we can see that there are considerable lateral variations in the velocity structure beneath China.

3.3 Resolution and accuracy

As we mentioned earlier, the 1-D velocity model at each point is inverted by the travel-time data inside a
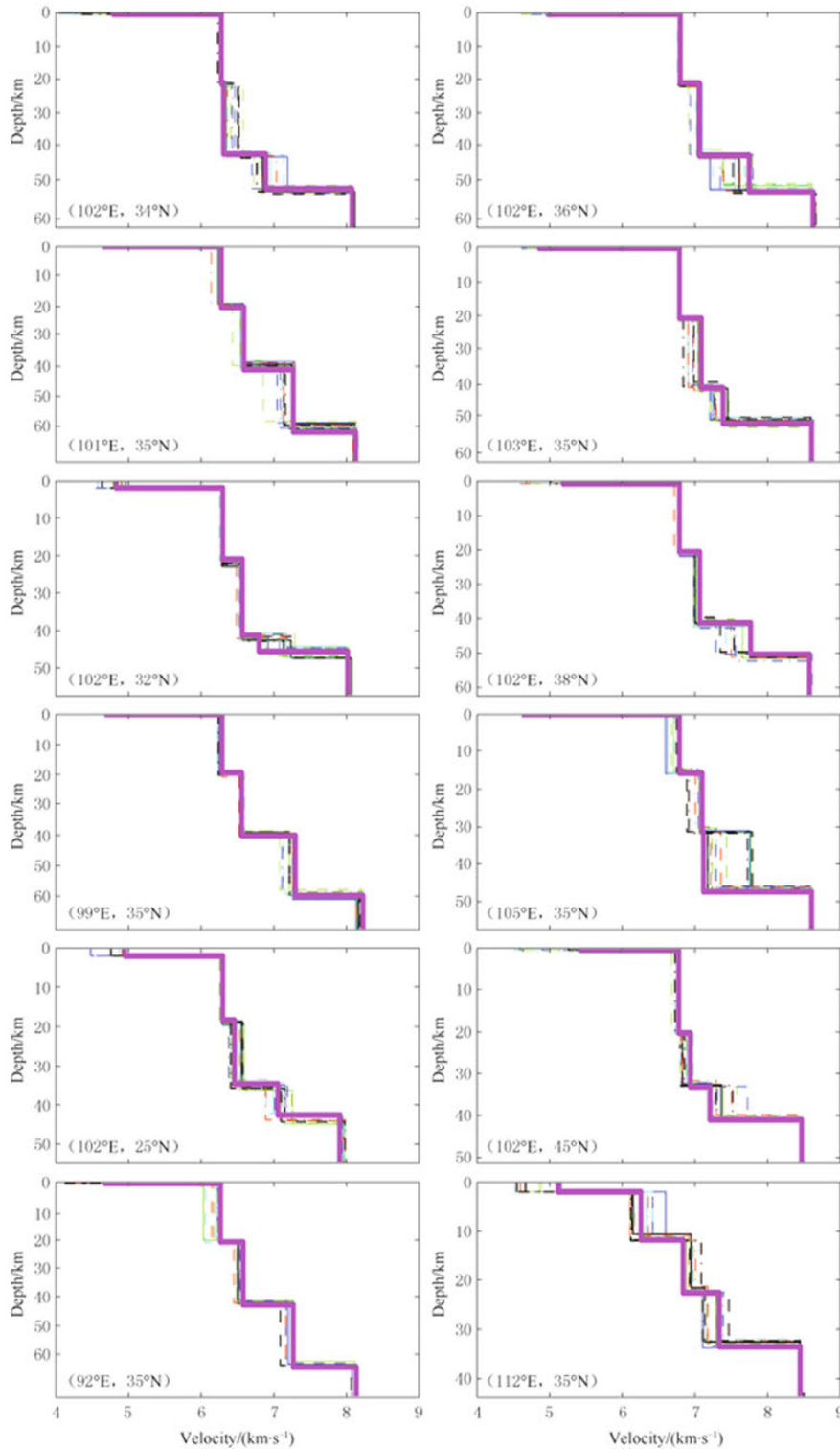
Figure 18   Ten best velocity models at the 12 selected locations shown in Figure 7. The final best velocity model with minimum RMS error at each location is shown in magenta.

window centered at that point. The size of the window depends on the number of arrivals of the ray paths in the window. The 1-D velocity model obtained at each point is an averaged layered model for the window. Therefore, even though the grid spacing between the selected points is $1°\times1°$, the size of the window indicates the
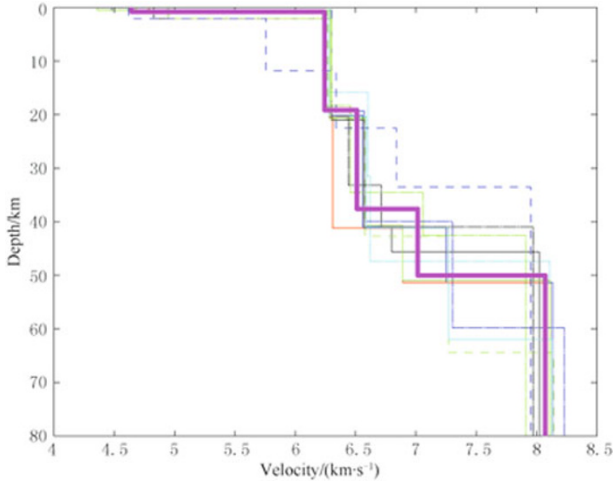
Figure 19 Best velocity models at the selected locations in Figure 7 and the best averaged velocity model in China (in magenta).

resolution of the model image. Smaller window sizes indicate higher resolution of the model image, and larger window sizes mean lower resolution of the model image.

The window-size distribution of all 2 600 points is shown in Figure 20a. About 80% of the region sizes are 8°×8° or smaller. Most areas with coarse ray coverage and large window size are in Mongolia and along the boundaries of the selected 2 600 points. Some parts of Tibet also require larger window sizes due to sparse station coverage.

Figure 20b shows the spatial resolution in terms of the normalized accuracy. We defined the accuracy in each window to be the number of selected ray paths divided by the window size. The normalized accuracy is obtained by dividing the accuracy of each window by the maximum accuracy in the China area. The normalized accuracy represents the inversion resolution in each window. We see a similar pattern between the window-size distribution and the resolution map.

3.4 Model comparison at the Moho interface

The models for comparison are CUB 1.0 (Shapiro and Ritzwoller, 2002), the SAIC 1°×1° model (Stevens et al., 2001), and CRUST 2.0 (Bassin et al., 2000). The first two models were constructed from the group and phase velocity dispersion measurements of surface waves. The last one was constructed from seismic refraction data, and was developed from the CRUST 5.1 model (Mooney, 1998) and 1°×1° sediment map (Laske and Masters, 1997).
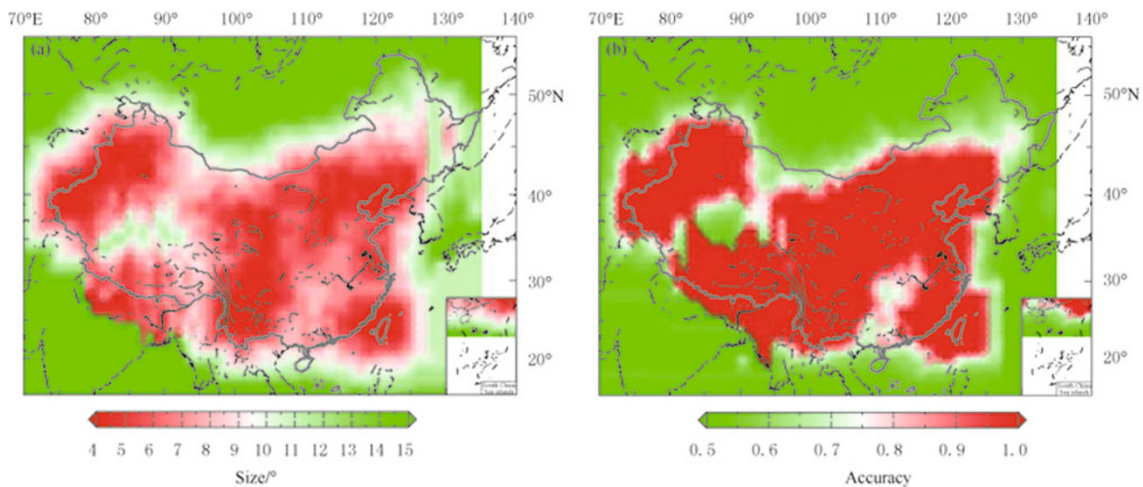

Figure 20 Window size distribution at all 2 600 points (a) and resolution (normalized accuracy) at all 2 600 points (b).

All the models show a good correlation with surface topography, with high elevation corresponding to a deep Moho (Figure 21). The outline of the Tibetan plateau is clearly depicted by all models. Though there are small differences, the large-scale features are similar in all the models, and Moho depth decreases from west to east in China. All of the models give the deepest

Moho (70+ km) at the center of the Tibetan plateau, and the shallowest (about 30 km) in the coastal areas around China's continental shelf.

The Moho depth (Figure 21) differences for all the models are shown in Figure 22. The difference is taken by subtracting the mean Moho depth for all models from each model. The Moho depth difference for most areas
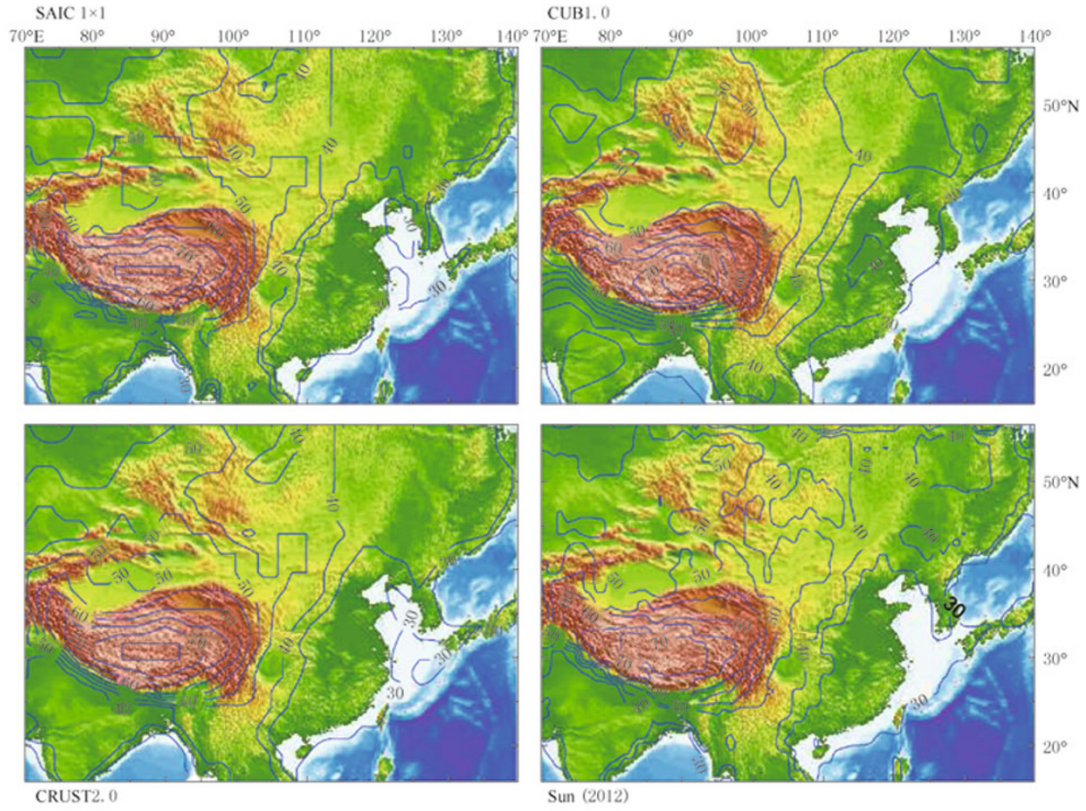
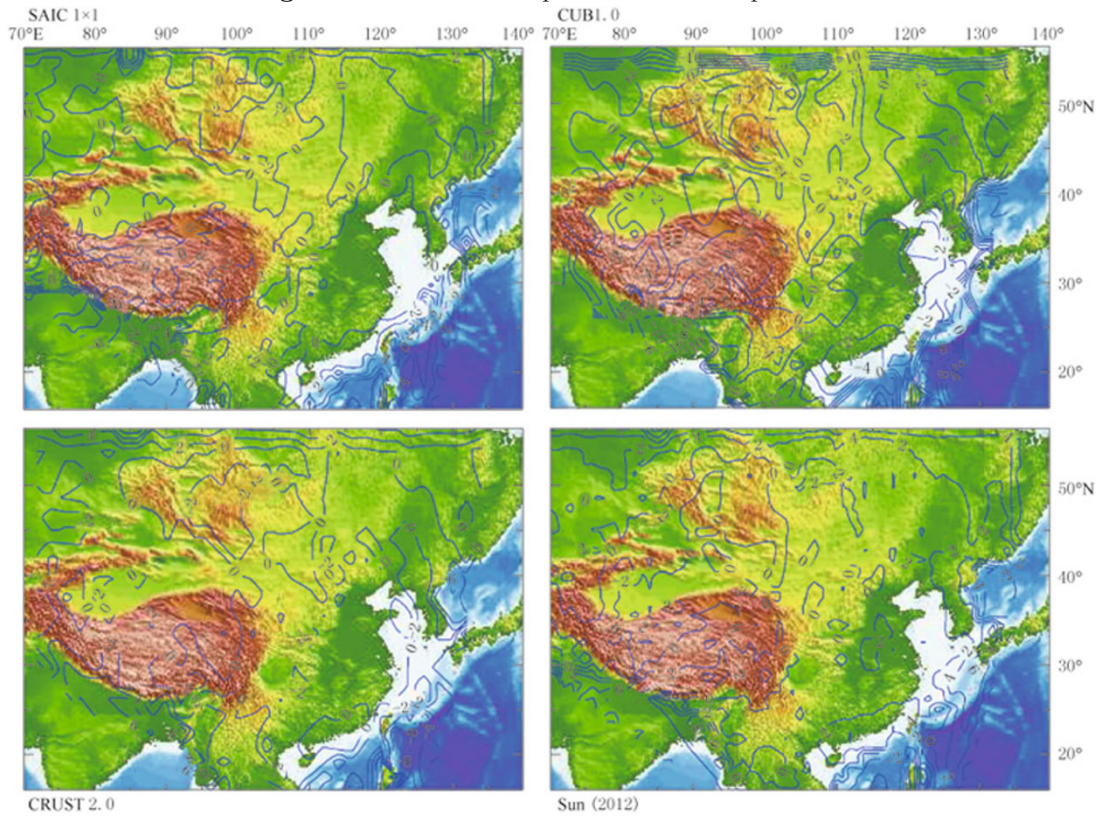**Figure 21**   Contour comparison of Moho depth.

Figure 22   Contour comparison of Moho depth difference. The difference is taken by subtracting the mean Moho depth of all models from each model. The Moho depth difference for most areas is close to zero.

is close to zero. In Mongolia and the area south of the Himalaya, the Moho depth differences are large. In Mongolia, only CUB 1.0 shows negative anomaly of the range from –10 km to –2 km. Sun (2012), SAIC and CRUST 2.0 show a positive anomaly in the range from 2 km to 4 km. In the area south of the Himalaya, both SAIC and CUB 1.0 show a strong negative anomaly from –10 km to –2 km, while Sun (2012) and CRUST 2.0 show a positive anomaly of 2 km to 6 km. The key differences lie in the southern Tianshan and central Tibet. Our model shows a 60 km Moho depth beneath Tianshan, about 10 km deeper than other models. Our model also shows a 78 km Moho depth beneath central Tibet, about 3–5 km deeper than other models.

The Pn model by Pei et al. (2007) was constructed directly from the Pn travel-times recorded in the China area (Figure 23). Due to Hearn's simple method, we believe that Pei's Pn model is the most accurate, and we took their model as a reference in our inversion. Thus, it is natural that our Pn model is similar to Pei's Pn model. There are large differences between the Pei's model and the two models based on surface waves. It

is not clear whether these differences emerge because of limited sensitivity of the surface wave to the thin layer of the upper mantle that defines Pn, or because the Pn velocity is obtained from the shear velocities of surface wave models. In any case, we believe that Pn velocities obtained directly from P-wave travel-times are more accurate than those of surface wave models.

3.5 Comparison of vertical crustal velocity profiles

Taking ten China Digital Seismograph Network stations (Figure 24) addressed in Mangino et al. (1999) as reference points, comparisons for 1-D vertical profiles are performed. Most stations shown in Figure 24 are in the regions with high ray density and good model accuracy (Figure 19).

The comparison is shown in Figure 25. The thick red lines indicate the results from our 1-D model. We can see that the differences from the other models are not very large at the reference points, even though the other models are obtained from diverse datasets. This supports the fact that our 1-D model is in general agreement with previous work.
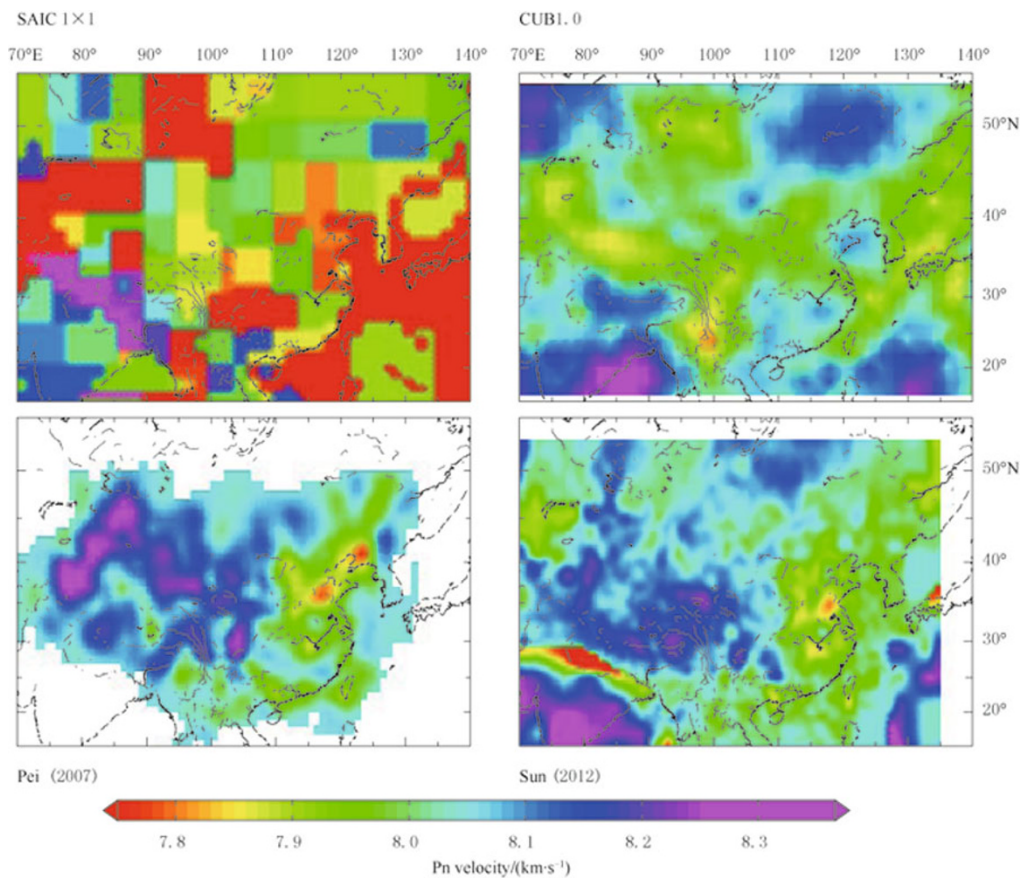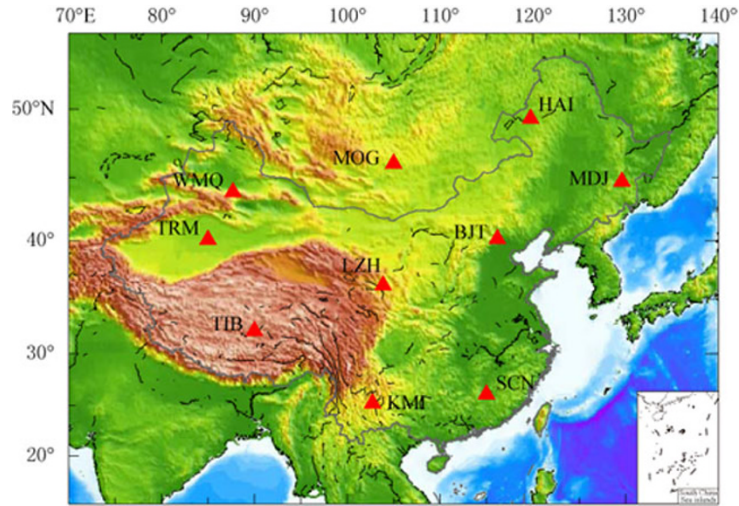

Figure 23   Pn velocity comparison.

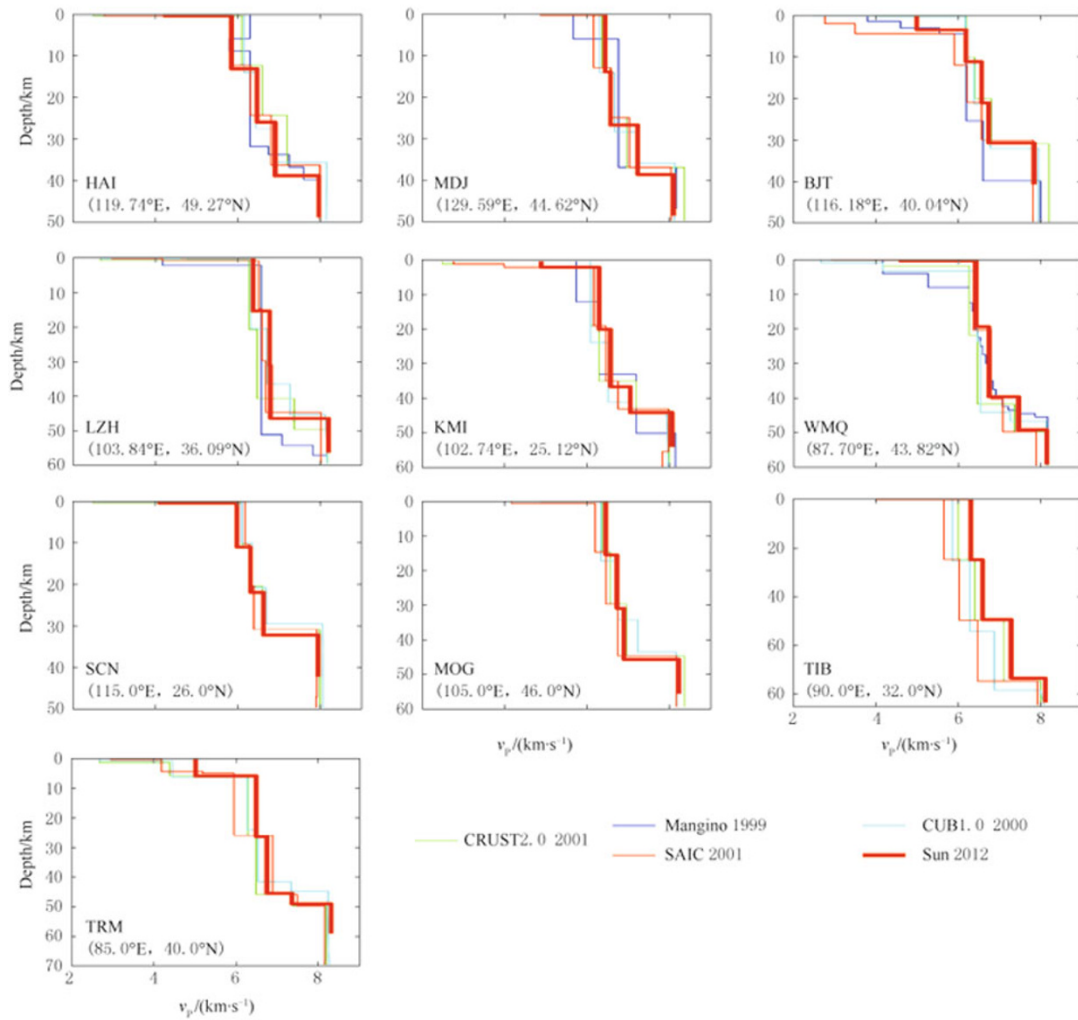**Figure 24**   Selected 10 locations for 1-D velocity comparison.

Figure 25   1-D velocity profile comparison at 10 locations in China. The thick red lines indicate the results of our 1-D model (Sun, 2012).

4 Discussion and conclusions

Our 1-D Monte Carlo inversion is performed for regions with sizes ranging from $4°×4°$ to $15°×15°$. Nearly 80% of the region sizes are $8°×8°$ or smaller. Due to the fact that adjacent 1-D velocity models are based on data with considerable overlap, a smooth transition from one velocity profile to adjoining profiles has been observed.

The earthquake source locations we used to construct the P-velocity models are the ones given in the *ABCE*. The location uncertainty may have an impact on our final velocity model. Since the ray paths at each selected location are dense, we believe the event location uncertainty does not play a significant role in each 1-D model inversion.

For the areas with coarse ray density, the window size goes up to $15°×15°$. The velocity models obtained in these regions are strongly averaged, have poor spatial resolution, and are less accurate compared to the ones in the areas with dense ray coverage. Most areas with coarse ray coverage are in Mongolia.

The Moho depths we obtained are similar to those in the CUB 1.0 (Shapiro and Ritzwoller, 2002), the SAIC $1°×1°$ (Stevens et al., 2001), and the CRUST 2.0 models (Mooney, 1998). All the models show excellent correlation between Moho depth and surface topography. However, our model shows more details and more accurate Moho depths in Tibet and Tianshan.

References

Bassin C, Laske G and Masters G (2000). The current limits of resolution for surface wave tomography in North America. *EOS Trans AGU* **81**: F897

Hearn T M, Wang S, Ni J F, Xu Z, Yu Y and Zhang X (2004). Uppermost mantle velocities beneath China and surrounding regions *J Geophys Res* **109**: B11301, doi:10.1029/2003JB002874.

Huang Z, Su W, Peng Y, Zheng Y and Li H (2003). Rayleigh wave tomography of China and adjacent regions. *J Geophys Res* **108**(B2): 2 073, doi 10.1029/2001JB001696.

Institute of Geophysics, China Seismological Bureau (IGCSB) (2000–2010). *Annual Bulletin of Chinese Earthquakes (ABCE)*. Seismological Press, Beijing (in Chinese).

Laske G and Masters G (1997). A global digital map of sediments thickness. *EOS Trans AGU* **78**: F483.

Lebedev S and Nolet G (2003). Upper mantle beneath southeast Asia from S velocity tomography. *J Geophys Res* **108**(B1): 2 048, doi 10.1029/2000JB000073.

Liang C, Song X and Huang J (2004). Tomographic inversion of Pn travel times in China *J Geophys Res* **109**: B11304, doi:10.1029/2003JB002789.

Liu F T, Wu H, Liu J H, Hu G, Li Q and Qu K X (1990). 3-D velocity images beneath the Chinese continent and adjacent regions. *Geophys J Int* **101**: 379–394.

Mangino S, Priestley K and Ebel J (1999). The receiver structure beneath the China digital seismograph network stations. *Bull Seismol Soc Am* **89**: 1 053–1 076.

McLeish A (1992). *Geological Science*. 2nd ed. Thomas Nelson & Sons., pp. 122.

Mooney W D (1998). CRUST 5.1: A global crustal model at $5°×5°$. *J Geophys Res* **103**: 727–747.

Monroe J S and Wicander R (2008). *The Changing Earth: Exploring Geology and Evolution*. 5th ed. Cengage Learning, pp. 216.

Pei S, Zhao J, Sun Y, Xu Z, Wang S, Liu H, Rowe C A, Toksöz M N and Gao X (2007). Upper mantle seismic velocities and anisotropy in China determined through Pn and Sn tomography. *J Geophys Res* **112**: B05312, doi:10.1029/2006JB004409.

Ritzwoller M H, Barmin M P, Villasenor A, Levshin A L and Engdahl E R (2002). Pn and Sn tomography across Eurasia to improve regional seismic event locations. *Tectonophysics* **358**(1-4): 39–55.

Shapiro N M and Ritzwoller M H (2002). Monte Carlo inversion for a global shear velocity model of the crust and upper mantle. *Geophys J Int* **151**: 88–105.

Song Z H, An C Q, Chen G Y, Chen L H, Zhuang Z, Fu Z W and Hu J F (1991). Study on 3-D velocity structure and anisotropy beneath the West China from the Love wave dispersion. *Acta Geophysica Sinica* **34**: 694–707 (in Chinese with English abstract).

Stevens J L, Adams D A and Baker G E (2001). Improved surface wave detection and measurement using phase-matched filtering with a global one-degree dispersion model In: *Proc. of 23rd Seismic Research Review: Worldwide Monitoring of Nuclear Explosions*. 2–5 October, Jackson Hole, Wyoming, 420–430.

Sun Y (2001). *Determination and Interpretation of Earthquake Source Locations in Sichuan Province, China*. [Master Dissertation]. MIT, Cambridge, Massachusetts.

Sun Y and Toksöz M N (2006). Crustal structure of China and surrounding regions from P-wave travel-

time tomography. *J Geophys Res* **111**: B03310, doi:10.1029/2005JB003962.

Sun Y, Kuleli S, Morgan F D, Rodi W and Toksöz M N (2004). Location robustness of earthquakes in Sichuan province, China. *Seism Res Lett* **75**(1): 54–62.

Wessel P and Smith W (1995). New version of the generic mapping tools released. *EOS Trans AGU* **76**: 329.

Wu F T, Levshin A L and Kozhevnikov V M (1997). Rayleigh wave group velocity tomography of Siberia, China and vicinity. *Pure Appl Geophys* **149**: 447–473.

Xu Y, Liu F, Liu J and Chen H (2002). Crust and upper mantle structure beneath western China from P wave travel-time tomography. *J Geophys Res* **107**(B10): 2 220, doi 10.1029/2001JB000402.